Nano Research

Open Access

Research Article

# Continuous production of bio-inspired hierarchical core–pith–sheath fiber electrodes for high performance fiber-shaped batteries

Chongyang Luo, Zhongwei Jiang, Ziqing Yao, Qingpeng Guo, Yujie Li, Weiwei Sun, Chunman Zheng ✉, and Shuangke Liu ✉

*National University of Defense Technology, Changsha 410000, China*

Cite this article: *Nano Research*, **2026**, *19*, 94908431. https://doi.org/10.26599/NR.2026.94908431

**ABSTRACT:** Wet-spinning is an effective and scalable continuous manufacturing process for fiber electrodes. However, fiber electrodes prepared by traditional wet-spinning often suffer from low mechanical strength and poor ionic/electronic conductivity. Inspired by the radially hierarchical structure of plant stems, we developed a coaxial wet-spinning technique based on a drawing-extrusion mechanism. By regulating the $Ca^{2+}$ concentration in the coagulation bath, a core–pith–sheath tri-layer architecture was constructed, which synergistically enhances mechanical strength and establishes efficient ionic transport pathways. Besides, a composite cathode consisting of $MnO_2$ nanosheets anchored on carbon nanotubes (CNTs) was synthesized, establishing a continuous electronic conducting network. The incorporation of dual conductive networks markedly enhanced the electrochemical and mechanical properties of the fiber electrodes. The fabricated fiber-shaped Zn–$MnO_2$ batteries (FZBs) delivered capacities of 343.5 mAh·g$^{-1}$ at 0.1 A·g$^{-1}$ and 144.7 mAh·g$^{-1}$ at 5 A·g$^{-1}$, respectively, along with excellent cycling stability—retaining 55.2% capacity after 5000 cycles at 5 A·g$^{-1}$ (an average per-cycle decay of 0.01%). Moreover, after 100,000 bending cycles at 2 A·g$^{-1}$, the capacity retention remained 74.9%. Furthermore, through tomography, electrochemical kinetics analysis, and ion-transport theoretical simulations, we elucidated the critical role of rapid ion migration within the porous pith layer in enabling high performance fiber batteries. The universality of this mechanism was further verified in aqueous fiber-shaped lithium-ion batteries. This work provides a scalable multilayer structural design strategy and theoretical foundation for the development of advanced fiber-based energy storage devices.

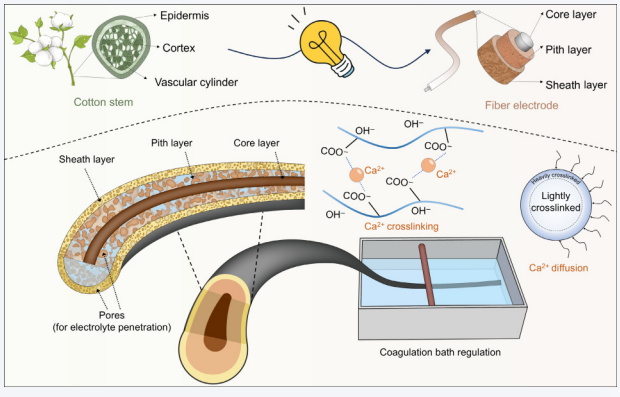


**KEYWORDS:** fiber-shaped batteries, $MnO_2$, wet-spinning, conductive network, porous structure

## 1 Introduction

Driven by advances in flexible electronics, artificial intelligence algorithms, and biosensing technologies, wearable devices have evolved into integrated systems encompassing medical healthcare, industrial safety, and consumer electronics, whose rapid development will significantly enhance the quality of human life [1]. Compared with conventional planar rigid batteries, fiber-shaped batteries possess superior deformability and weavability, making them more suitable as flexible power sources for wearable devices [2]. Among various types of fiber-shaped batteries, aqueous zinc-based batteries emerge as the most promising candidates due to their high specific capacity, intrinsic safety, and cost-effectiveness [3]. Notwithstanding these benefits, the practical implementation of fiber-shaped zinc-ion batteries (ZIBs) is impeded by two significant obstacles. (1) Electrode fabrication: Existing methods for electrode preparation, such as hydrothermal synthesis [4], electrodeposition [5], and solution-based reactions [6], are generally discontinuous and limited in scale, rendering them unsuitable for the requirements of scalable, continuous production in industrial contexts. (2) Performance enhancement: Recurring challenges that frequently afflict planar Zn-based batteries, such as zinc dendrite

**Received:** November 9, 2025; **Revised:** December 20, 2025
**Accepted:** January 12, 2026

✉Address correspondence to Chunman Zheng, zhengchunman@nudt.edu.cn; Shuangke Liu, liu_sk@139.com

formation [7], cathode degradation [8], and side reactions of electrolyte [9], are similarly evident in fiber systems. Moreover, the intrinsic curvature of fiber electrodes intensifies these problems, resulting in significant polarization and inferior electrochemical performance [10].

Significant efforts have been undertaken by researchers to tackle these difficulties. Techniques, such as wet spinning and extrusion-based three-dimensional (3D) printing, are explored as viable methods for continuous fiber electrode fabrication [11–14]. In addition, various optimization strategies are implemented, including the anode design [15, 16], the cathode modifications [17, 18], and the electrolyte additives [19, 20]. Notwithstanding these developments, attaining both continuous manufacturing and exceptional electrochemical performance continues to pose a considerable difficulty. On the one hand, in continuous fabrication, ensuring fiber strength frequently necessitates a compromise in electrochemical performance [21]. On the other hand, Certain continuous production processes necessitate special criteria regarding the inherent physical features of materials, including the liquid-crystalline behavior of dispersions [22].

Among various scalable manufacturing methods, wet-spinning emerges as an attractive technology due to its simplicity, high efficiency, and appropriateness for continuous production. A spinning solution is extruded through a spinneret into a coagulation bath, leading to solidification and precipitation to produce fibers. This method has been widely employed to fabricate functional fibers with diverse architectures, such as coaxial, parallel, and twisted configurations, for energy storage devices [23]. However, three major limitations hinder the electrochemical performance of wet-spun fiber electrodes: (1) The current collector is frequently arranged by winding around the fiber post-fabrication, which constrains effective radial electron transport throughout the fiber; (2) many current methods depend on the basic physical amalgamation of electrode and conductive materials, neglecting to establish a continuous and resilient electronic conduction network; and (3) the densification of the electrode under rapid forming conditions impedes electrolyte penetration, obstructing the formation of effective ionic transport channels. Therefore, tackling these issues primarily relies on rational design strategies that entail the creation of continuous ionic routes and interconnected electronic networks. Although strategies for shortening conduction pathways, such as spraying conductive carbon layers [24], wrapping carbon nanotube (CNT) films [25], and multi-strand assembly designs [26] were employed, these methods often involved complex processing steps and low production efficiency. Thus, developing a simple yet effective method to establish efficient electronic/ion conductive pathways with mechanical strength for fiber electrodes remains a formidable challenge.

Hierarchical fiber design has been acknowledged as an efficacious approach for fulfilling multiple performance criteria [27]. For example, Wu et al. [28] integrated protective support and enhanced electrical conductivity by designing hierarchical core–sheath fibers. Yu et al. [29] fabricated aerogel fibers with a porous sheath–dense core structure, enabling fibers to exhibit high tensile strength and low thermal conductivity. Zheng et al. [30] developed a core–sheath conductive fiber in which the outer fluorinated elastomer layer provided protection and elasticity, while the inner liquid-metal-containing core ensured stable electrical conductivity under tensile deformation. However, the integration of such coaxial structures often relies on multistep fabrication processes and the combination of multiple materials to achieve functional integration.

Herein, inspired by the hierarchical architectures of plant stems, we fabricated fiber electrodes with a three-layer architecture (core–pith–sheath) via a coaxial wet-spinning process based on the fiber-forming principle. The dense sheath layer efficiently mitigates swelling and guarantees the structural integrity of the fiber. The porous pith layer enables electrolyte penetration and offers effective ion-transport pathways. The current-collector core layer facilitates swift electron transportation and improves the mechanical integrity of the fiber. Significantly, neither multistep processing nor various materials is requisite for the construction of this hierarchical system. This design enhances battery performance by integrating synergistic functionality across many hierarchical layers, providing insights for next-generation multilayer fiber electrode development.

As a result, the presence of the sheath layer reduced the swelling in the electrolyte and effectively improved the structural stability of the fiber electrode. The incorporation of the core layer enhanced tensile strength by more than 44 times and significantly diminished polarization. The porous pith layer facilitated swift electrolyte infiltration, establishing uninterrupted ionic conduction routes that diminish charge-transfer resistance by about eight times in comparison to non-optimized electrodes. Accompanied by a composite cathode (resistivity diminishes from 78.17 to 0.03 $k\Omega \cdot cm^{-1}$), the fabricated fiber-shaped Zn–$MnO_2$ batteries (FZBs) exhibited remarkable electrochemical performance. Their discharge specific capacities were 343.5 $mAh \cdot g^{-1}$ at 0.1 $A \cdot g^{-1}$ and 144.7 $mAh \cdot g^{-1}$ at 5 $A \cdot g^{-1}$, with a capacity retention of 55.2% after 5000 cycles at 5 $A \cdot g^{-1}$ (average decay rate of 0.01% per cycle). Besides, the structural stability of the designed fibers provided FZBs with exceptional mechanical flexibility, ensuring consistent discharge performance across bending angles ranging from 0° to 120°. After 100,000 bending cycles at 2 $A \cdot g^{-1}$, the capacity retention was 74.9%. Furthermore, both the individual FZBs and the woven energy fabrics demonstrated steady performance under sunlight exposure, water immersion, and mechanical cutting, indicating robustness and suitability for next-generation wearable energy storage devices.

## 2 Results and discussion

### 2.1 Structural design and fabrication process of fiber electrodes

Figure 1 illustrates the design inspiration of the fiber electrode structure. Inspired by the hierarchical organization of plant stems—taking cotton stems as an example—the primary structure can be divided into three layers (Fig. 1(a)): the epidermis, which protects the internal tissues from mechanical damage, pests, and water loss; the cortex, which provides elasticity and supports the upright growth of young stems; and the vascular cylinder (containing vascular bundles, pith, and pith rays), which functions in the transport and storage of water and nutrients. These three layers act synergistically to ensure the stable growth of cotton plants in natural environments. Analogously, the fiber electrode designed in this work consists of three functional layers (Fig. 1(b)). The moderately dense sheath layer maintains the structural integrity of the electrode, preventing dispersion in electrolyte immersion (Fig. S1 and Video S1 in the Electronic Supplementary Material (ESM)). The pith layer, characterized by a loose and porous structure,

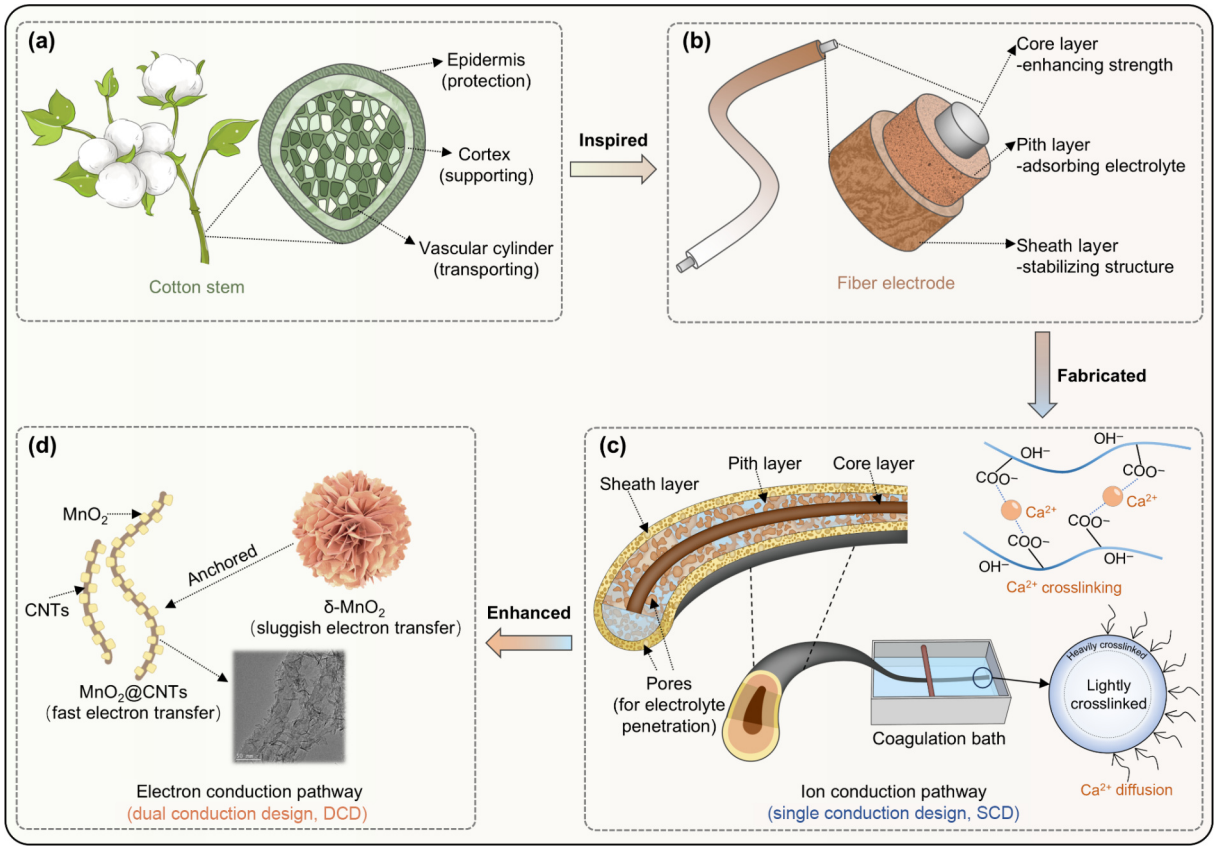


**Figure 1** Schematic diagram illustrating the design concept of bio-inspired fiber electrodes. (a) Three-layer structure of the cotton stem. (b) Three-layer structure of the hierarchical fiber electrode. (c) Process mechanism for constructing SCD structure. (d) Material compositing for constructing the DCD structure.

promotes electrolyte infiltration and diffusion. The core layer, composed of a metallic current collector, serves as a mechanical backbone that significantly enhances tensile strength and simultaneously collects and transfers electrons efficiently, thereby reducing battery polarization. Together, these three layers form integrated pathways for ionic and electronic conduction, enabling the fiber electrodes to achieve superior electrochemical performance and keep structural stability.

This multilevel hierarchical architecture is realized through a coaxial wet-spinning process, in which the structure formation is controlled by tuning the $Ca^{2+}$ concentration of the coagulation bath. $Ca^{2+}$ can interact with the $-COO^-$ groups on CMC (carboxymethylcellulose) chains through ionic bonding, thereby bridging multiple CMC chains to form an ordered three-dimensional crosslinked network. This crosslinking mechanism is analogous to that observed in sodium alginate systems, which are likewise rich in carboxyl groups [31]. Previous studies have demonstrated that divalent metal ions, such as $Ca^{2+}$ and $Zn^{2+}$, can induce the formation of coordination crosslinked networks in CMC [32], and this mechanism has been widely employed in the fabrication of CMC-based hydrogels and fibers. For instance, Bai et al. [33] prepared high-strength hydrogels via $CaCl_2$ crosslinking and elucidated the underlying calcium-ion-induced crosslinking mechanism. Similarly, Wang et al. [34] fabricated CMC-based fibrous supercapacitors using a 5 wt.% $CaCl_2$ coagulation bath.

The formation of the pith–sheath structure primarily arises from calcium-ion-induced crosslinking in combination with diffusion differences within the coagulation bath. Upon the extrusion of the CMC spinning solution into the coagulation bath, solvent exchange transpires initially, resulting in the preliminary creation of the fiber, while $Ca^{2+}$ concurrently diffuses into the interior of fiber. The outside part of the fiber first contacts coagulation bath, leading to fast densification due to elevated local ion concentration. This dense outer layer impedes further inward diffusion of the coagulation bath, thereby reducing the gelation rate of the inner region and ultimately resulting in a typical pith–sheath structure characterized by a dense exterior and a loose interior [35]. This internal porosity enables thorough electrolyte infiltration, establishing ionic conduction pathways, which are herein referred to as single-conductive design (SCD, Fig. 1(c)). To further enhance electronic conductivity, $MnO_2$ nanosheets were *in situ* grown on CNTs, forming a continuous electron transport network. The integration of this electron-conductive network with the pre-existing ionic-conductive channels results in a dual-conductive design (DCD, Fig. 1(d)), which synergistically optimizes both ion and electron transport within the fiber electrodes.

Fibers produced by conventional wet-spinning lack sufficient strength and require external wrapping with a current collector to export electrons. In this work, high-conductivity and high-mechanical-strength metal wires are integrated as the core, enabling the overall fiber electrode to achieve high mechanical strength and efficient electron transport. As illustrated in Fig. 2(a), the fabrication process of the fiber electrode involved simultaneous extrusion of the electrode slurry and collection of a stainless-steel current collector, thereby ensuring uniform loading of the slurry onto the collector surface. During the process, the dispersion solvent in the slurry diffuses and undergoes phase transformation in the coagulation bath due to concentration gradients. Under the coordination of

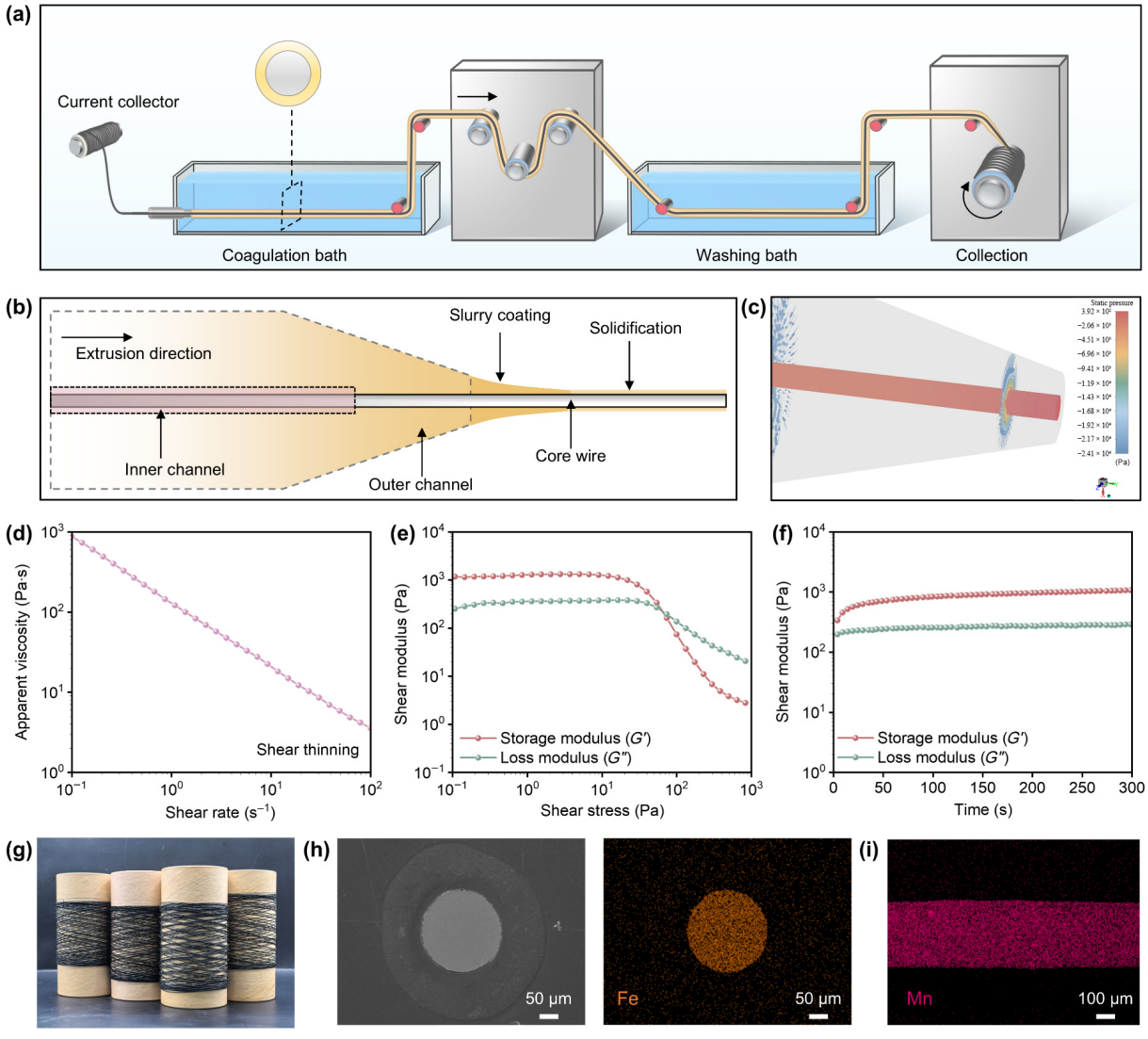


**Figure 2** Fabrication process of hierarchical fiber electrodes. (a) Schematic diagram of the fiber electrode preparation process. (b) Schematic diagram of the slurry loading process. (c) Simulation of the slurry loading process. (d) Relationship between apparent viscosity and shear rate. (e) Relationship between *G*' and *G*" with shear stress. (f) Variation of *G*' and *G*" over time. (g) Optical photograph of continuously prepared fiber electrodes. (h) SEM and EDS of the cross-sectional fiber electrode. (i) EDS of fiber electrode surface.

metal ions, the electrode slurry crosslinks and solidifies into a fiber electrode. The as-formed fibers were then rinsed in a washing bath to remove residual metal ions and subsequently collected for use.

Maintaining uniformity of the load during this synchronous stretching process is a major challenge, which requires attention to both the structural design of the needle and the rheological properties of the slurry. Figure 2(b) shows the slurry loading process during fiber drawing. Owing to its high viscosity (Fig. S2 in the ESM), the slurry continuously coated the moving current collector and rapidly solidified to maintain its structural integrity. To achieve uniform slurry loading, a custom-designed concave conical nozzle was employed in this study. This tapered geometry results in higher outlet velocity and increased shear stress, which facilitates fiber formation. As shown by the simulation in Fig. 2(c), the slurry velocity directed toward the core filament increased as the outlet diameter decreased, generating higher local pressure near the filament surface and promoting firm adhesion of the slurry. Near the outlet, the slurry velocity adjacent to the filament wall was slightly higher than the feeding speed but overall remains consistent with it, indicating uniform attachment of the slurry to the filament and ensuring excellent homogeneity of the fiber electrodes (Fig. S3 in the ESM).

Rheological analysis further confirms the stability and continuity of the fiber-forming process. The slurry exhibited a typical shear-thinning behavior, and its sufficiently high zero-shear viscosity ensured good extrudability and shape retention during spinning, critical for continuous wet-spinning operations (Fig. 2(d)). The essence of fiber production involves extruding polymer solution through a spinneret to form continuous fibers, a procedure that necessitates overcoming the internal friction of fluid, which is its viscosity. Shear-thinning behavior significantly reduces the processing difficulty by dynamically regulating the viscosity during extrusion. Specifically, a shear-thinning spinning solution maintains a relatively low viscosity under the high shear conditions inside the spinneret, which facilitates continuous and uniform extrusion. Once extruded from the spinneret, the viscosity rapidly recovers to a higher value, which is favorable for maintaining fiber integrity and enabling subsequent fiber formation [36, 37].

In contrast, as shown in Fig. S4 in the ESM, a spinning solution without shear-thinning behavior can be classified into two extreme cases. In the first case, the spinning solution exhibits an excessively high viscosity, requiring a large driving force for extrusion and often leading to accumulation and clogging within the spinneret channel. Even extruded, the nonuniform extrusion speed can cause the solution to break into droplets.

In the second case, the spinning solution has an extremely low viscosity (e.g., water). Although such fluids can be easily extruded, they immediately disperse upon exiting the spinneret and are unable to retain a stable fibrous morphology.

The relationship between storage modulus ($G'$), loss modulus ($G''$), and shear stress indicates that below the yield stress ($G' > G''$), the slurry behaves elastically like a solid. Once the yield point is exceeded, $G'$ rapidly decreases and becomes lower than $G''$, signifying a transition from solid-like to liquid-like behavior due to network rupture induced by viscous deformation (Fig. 2(e)). These unique rheological features ensure that the slurry can be smoothly extruded through the fine nozzle under pressure while maintaining fiber integrity within the coagulation bath during continuous spinning. Moreover, the slurry exhibited excellent rheological stability, with $G'$ and $G''$ remaining nearly constant over time (Fig. 2(f)). As shown in Fig. 2(g), the optical photograph of the continuously prepared fiber electrodes is presented. Based on the surface and cross-sectional scanning electron microscopy (SEM) and energy dispersive X-ray spectroscopy (EDS) analyses, it can be observed that the slurry was uniformly loaded onto the stainless-steel wire (Figs. 2(h) and 2(i) and Fig. S5 in the ESM).

### 2.2 Structural evolution under different coagulation bath conditions

As shown in Fig. S6 in the ESM, cross-sectional SEM images illustrate the morphology of the fiber electrodes fabricated under different coagulation bath concentrations (1 wt.%, 3 wt.%, and 5 wt.%), denoted as 1%-coagulation bath fiber (1%-CBF), 3%-CBF, and 5%-CBF, respectively. The 1%-CBF exhibited a clear sheath–pith structure, consisting of a thin, dense sheath layer and a loose, porous pith layer. In contrast, both 3%-CBF and 5%-CBF showed reduced porosity, with indistinct boundaries between inner and outer regions. The observed difference originates from the $Ca^{2+}$-dependent crosslinking density. During rapid solvent exchange, a high ion concentration in the coagulation bath accelerates polymer crosslinking, resulting in overall fiber densification. In contrast, at low ion concentrations, most $Ca^{2+}$ ions were consumed in forming the outer dense sheath, and the remaining ions induce only weak crosslinking within the polymer matrix. The magnified view of the inner region further reveals that 3%-CBF and 5%-CBF contain only a few weakly crosslinked areas (porous area), which make it difficult for electrolyte infiltration and diffusion. In comparison, 1%-CBF maintained a uniformly porous interior, which favors ion transport.

To more convincingly demonstrate the existence of the dense sheath layer, we subsequently prepared thinly coated fiber electrodes to facilitate cutting down to the core current collector. Focused ion beam (FIB) milling was then employed to achieve precise sectioning. Through the physical sputtering effect induced by high-energy ion bombardment, the material was removed layer by layer, enabling the acquisition of a clean and neat cross-section (Fig. S7 in the ESM). As shown in Fig. 3(a), a well-ordered cross-sectional morphology from the surface to the inner core layer can be clearly observed. The outer sheath layer is dense, while the intermediate pith region exhibits abundant pores, which is fully consistent with the proposed core–pith–sheath structural model. Another piece of evidence for this structure is the $Ca^{2+}$ distribution across the fiber cross-section. As shown in Fig. 3(b), from the inner pith region toward the outer sheath layer, the calcium-ion content exhibits a clear increasing trend. This indicates that there is a different crosslinking density between the pith and sheath layer.

As shown in Fig. 3(c), surface wettability varied significantly with coagulation bath concentration. Owing to its lower crosslinking degree and higher surface roughness, 1%-CBF exhibited the smallest static contact angle (88°), while those of 3%-CBF and 5%-CBF are 97° and 111°, respectively. This obviously indicates that 1%-CBF possesses the highest hydrophilicity and electrolyte affinity among the three samples.

Micro-computed tomography (Micro-CT) was employed to nondestructively analyze the internal structure of the fibers. As shown in Fig. 3(d)(i), bright regions correspond to densely crosslinked aggregates of $MnO_2$, binders, and conductive additives. In 5%-CBF, large, highly crosslinked agglomerates were distinctly visible, forming massive clusters throughout the electrode. In 3%-CBF, the degree of crosslinking was moderate, with smaller particles and occasional microvoids. By contrast, 1%-CBF showed finely dispersed aggregates uniformly distributed within the electrode and abundant microporous regions. Three-dimensional reconstruction of the internal structure based on grayscale segmentation (Fig. S8 in the ESM) divides the electrode into low-, middle-, and high-density regions [38]. The low-density zones represent pores and weakly crosslinked regions that facilitate electrolyte permeation, while high-density regions correspond to strongly crosslinked polymer domains that block ionic transport.

In Fig. 3(d)(ii), the reconstructed images clearly show that both 3%-CBF and 5%-CBF contained extensive high-density regions near the surface, indicating a compact and smooth morphology. In contrast, 1%-CBF displayed fragmented high-density regions distributed across a rougher surface, confirming its higher porosity and improved electrolyte wettability. Quantitative analysis revealed that 1%-CBF had the highest proportion of low-density regions (58%), while 5%-CBF showed the lowest (49%), verifying that increasing coagulation bath concentration leads to higher crosslinking density and reduced porosity (Fig. 3(d)(iii)).

Two critical parameters govern the electrochemical performance of cathode materials: (1) the specific surface area, which determines ion/electron diffusion length and thus rate capability, and (2) the electrical resistivity, which affects charge transport and polarization behavior. In this work, composite cathode materials with varying ratios of $KMnO_4$ to CNTs were synthesized to investigate these factors systematically.

As shown in Fig. S9 in the ESM, SEM images display the morphologies of the obtained $MnO_2$@CNTs composites, denoted as δ-$MnO_2$ (without CNTs), M@C-2.5, M@C-5, and M@C-10. For M@C-2.5 ($KMnO_4$:CNT = 2.5:1), $MnO_2$ nanosheets were uniformly grown on CNT surfaces. As $KMnO_4$ concentration increased (M@C-5), thicker nanosheets were formed with alternating thin and thick regions. At even higher ratios (M@C-10), the product predominantly consisted of thick $MnO_2$ nanosheets, along with excess δ-$MnO_2$ nanoflowers of poor conductivity. These morphological variations were further confirmed by transmission electron microscopy (TEM) analysis (Fig. S10 in the ESM). The morphology strongly influenced the specific surface area of the composites (Fig. S11 in the ESM). M@C-5 exhibited a slightly

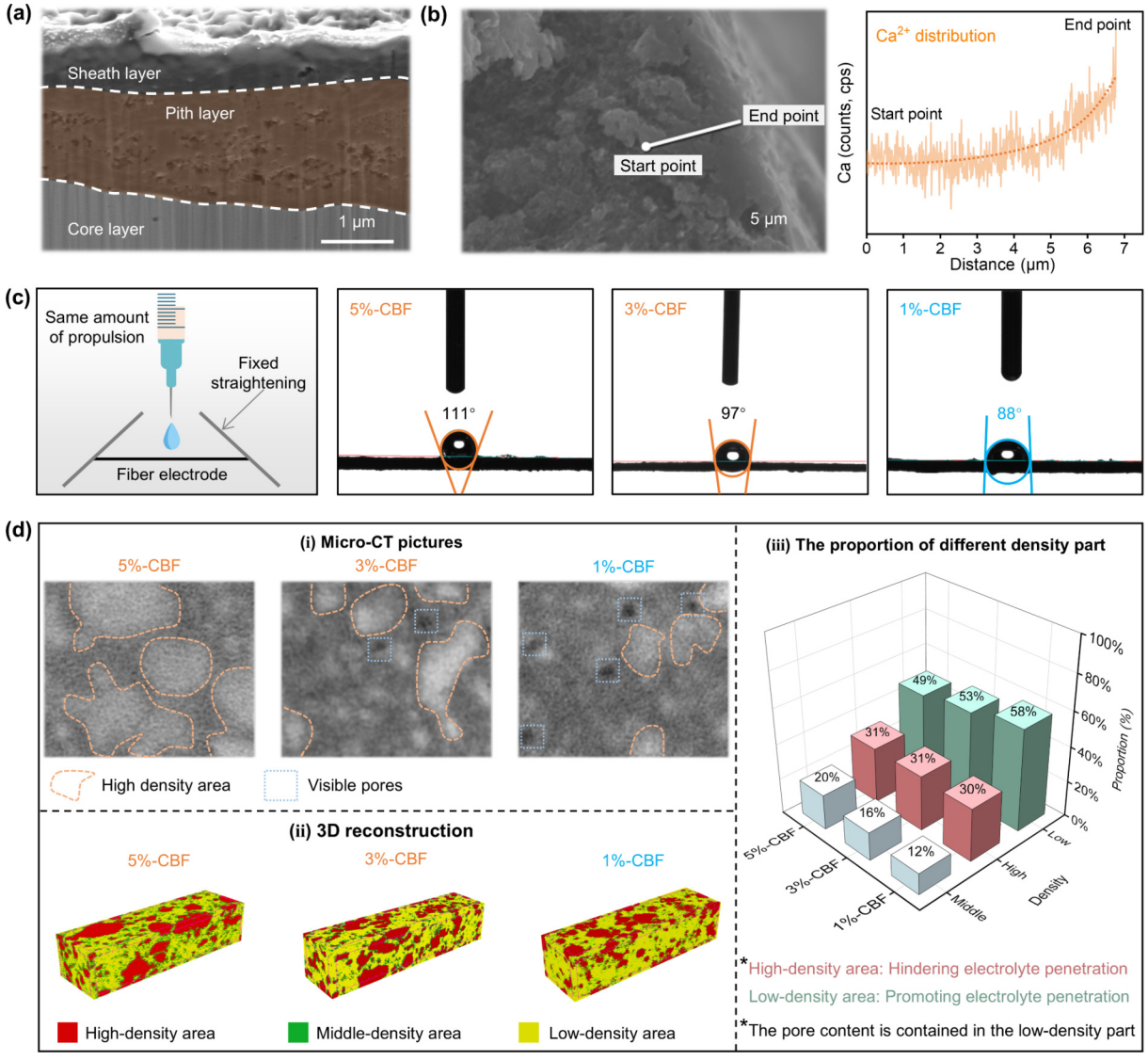


**Figure 3** Characterization of hierarchical fiber electrodes under different coagulation baths. (a) Cross-sectional SEM of fiber electrode after FIB milling. (b) EDS line scanning of $Ca^{2+}$ on the cross-section of the fiber electrode. (c) Surface contact angle of fiber electrode. (d) Micro-CT results of fiber electrode: (i) Micro-CT images, (ii) 3D reconstruction, and (iii) proportion of various density components.

higher surface area (226.4 $m^2 \cdot g^{-1}$) due to the coexistence of thick and thin nanosheets. However, further increasing the $KMnO_4$ ratio to M@C-10 resulted in complete occupation by thick nanosheets, leading to the lowest surface area (191.3 $m^2 \cdot g^{-1}$). Additionally, steric hindrance from thick nanosheets reduced pore diameter, whereas M@C-2.5 showed the largest pore size (16.5 nm, Fig. S12 in the ESM) and a relatively high surface area (214.0 $m^2 \cdot g^{-1}$), favoring electrolyte infiltration and providing abundant active sites for electrochemical reactions. X-ray diffraction (XRD) confirmed that synthesized cathodes are δ-$MnO_2$ (Fig. S13(a) in the ESM), showing characteristic diffraction peaks at 12.5° (001), 25.2° (002), 36.2° (100), and 65.6° (110) [39, 40]. The Mn 2p X-ray photoelectron spectroscopy (XPS) spectra displayed a typical spin-orbit splitting of ~ 12 eV between Mn $2p^{1/2}$ and Mn $2p^{3/2}$, indicative of $Mn^{4+}$ oxidation states (Fig. S13(b) in the ESM).

However, the $MnO_2$ content varied with the $KMnO_4$:CNT ratio, influencing the electrical conductivity. As shown in Fig. S14 in the ESM, the Raman peaks of CNTs gradually diminished with increasing $KMnO_4$ concentration, indicating that the CNT framework becomes progressively covered by $MnO_2$. Thermogravimetric analysis (Fig. S15 in the ESM) further supported this analysis. M@C-10 possessed the highest $MnO_2$ content, as reflected by the lowest weight loss under identical conditions. Since CNTs provided the primary electronic conduction pathways, excessive $MnO_2$ deposition lowered the overall conductivity of the composites. As shown in Fig. S16 in the ESM, the compacted powder resistivities followed the order: M@C-2.5 (0.03 kΩ·$cm^{-1}$) < M@C-5 (1.56 kΩ·$cm^{-1}$) < M@C-10 (4.27 kΩ·$cm^{-1}$) < δ-$MnO_2$ (78.17 kΩ·$cm^{-1}$). After being integrated into fiber electrodes (Fig. S17 in the ESM), M@C-2.5 maintained the lowest resistivity (12 mΩ·$cm^{-1}$).

To validate the performance correlation, M@C-5 (fabricated under 1% coagulation bath) was selected for comparison. Its discharge specific capacity reached only 142.2 mAh·$g^{-1}$ at 0.5 A·$g^{-1}$, with 69.3% capacity retention after 200 cycles (Fig. S18 in the ESM). Nevertheless, due to its relatively large surface area and moderate resistivity, M@C-5 still exhibited stable charge–discharge plateaus after multiple cycles. This behavior was absent in low-conductivity

materials, such as δ-$MnO_2$, employed in single-conductive networks (detailed in the SCD performance). These results clearly demonstrate the importance of constructing composite conductive materials and ionic transport networks to achieve superior electrochemical performance.

### 2.3 Ion transport mechanism and electrochemical performance correlation

The disparity in electronic conductivity can be directly assessed by resistivity tests; however, quantifying the ionic conductivity of fiber electrodes poses greater challenges. Our analysis revealed that establishing an efficient ionic conduction network is more critical than electronic conduction; fiber electrodes devoid of ionic routes were virtually incapable of performing standard charge–discharge procedures. To clarify this mechanism, we chose the samples exhibiting the most pronounced porosity (1%-CBF and 5%-CBF) for comparison investigation, emphasizing the significance of ionic transport in influencing electrochemical performance. The selection range of the model was the area from the dense sheath layer on the surface to the pith layer. The wettability and electrolyte infiltration dynamics were simulated as shown in Fig. 4(a). Due to its dense sheath and low internal porosity, the electrolyte could wet only 28% of the 5%-CBF fiber within 30 μs, whereas the 1%-CBF was completely infiltrated within the same time frame. The infiltration rate–time curves (Fig. 4(c)) reveal that 1%-CBF exhibited a significantly higher infiltration rate than 5%-CBF, consistent with their electrochemical impedance results. 5%-CBF charge-transfer resistances exceeded 1500 Ω (Fig. S19 in the ESM).

During actual charge–discharge processes, $Zn^{2+}$ migrates under both diffusion and electric field-driven migration. The distributions

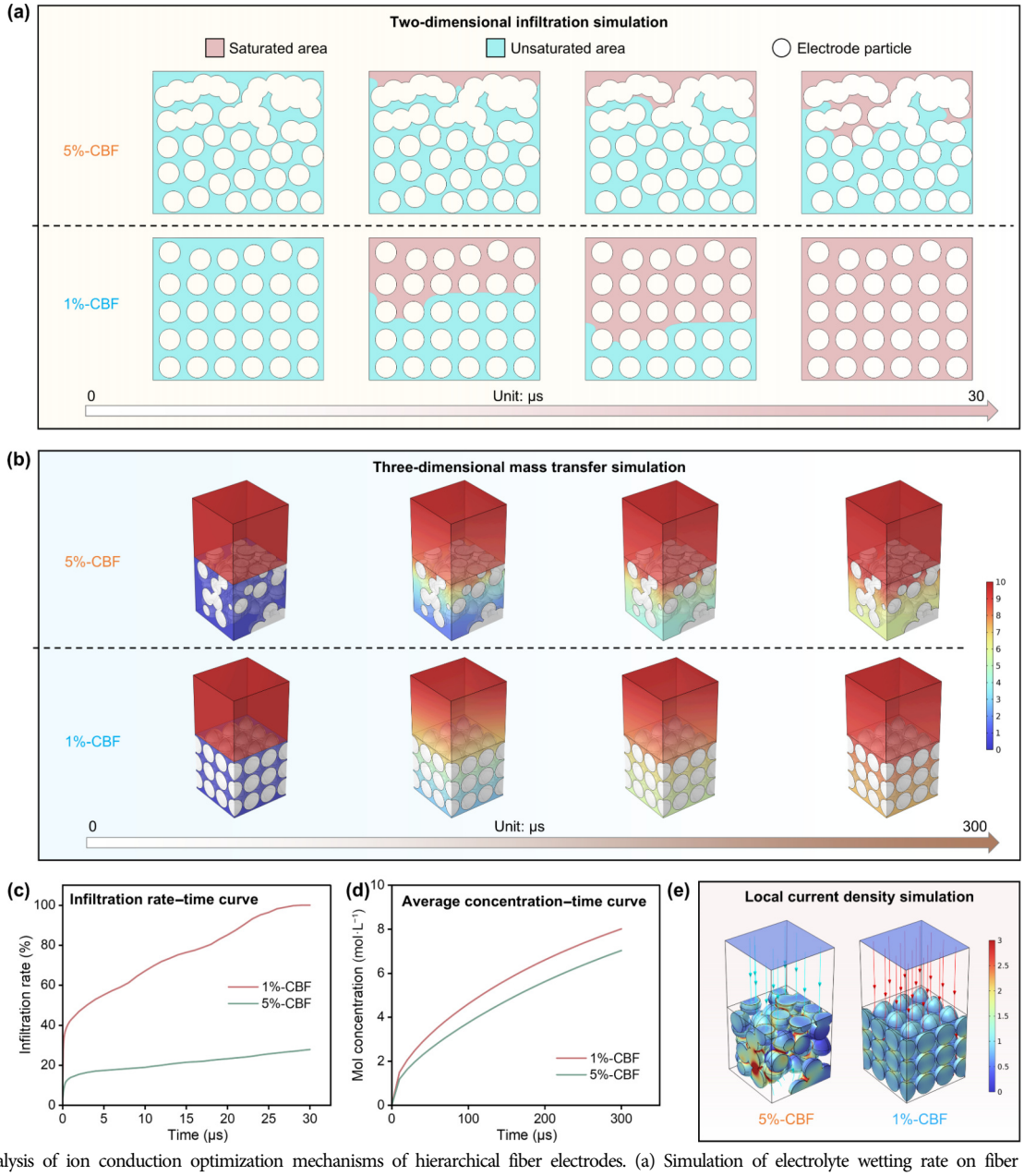


**Figure 4** Analysis of ion conduction optimization mechanisms of hierarchical fiber electrodes. (a) Simulation of electrolyte wetting rate on fiber electrodes. (b) Simulation of zinc ion mass transfer within fiber electrodes. (c) Infiltration rate–time curves. (d) Average concentration-time curves. (e) Simulation of local current density in fiber electrodes.

of $Zn^{2+}$ content in the two types of electrodes were compared (Fig. 4(b)). The 5%-CBF displayed a pronounced vertical concentration gradient, with much lower $Zn^{2+}$ concentration in the inner regions than near the surface, leading to severe concentration polarization and rapid attainment of the cutoff voltage, thereby reducing the discharge capacity. In contrast, 1%-CBF maintained a uniform electrolyte concentration throughout the electrode over time, with a smaller concentration difference between its inner and outer regions. As shown in Fig. 4(d), the average $Zn^{2+}$ concentration-time profiles further indicate that 5%-CBF consistently maintains a lower ion concentration during the entire mass-transfer process.

To quantify ion migration ability, the galvanostatic intermittent titration technique (GITT) was analyzed (Fig. S20 in the ESM). The $Zn^{2+}$ diffusion coefficients of 1%-CBF and 5%-CBF were $2.07 \times 10^{-11}$ and $4.95 \times 10^{-12}$ $cm^2 \cdot s^{-1}$, respectively, demonstrating that 1%-CBF achieves an order-of-magnitude improvement in ionic diffusivity. Moreover, under identical GITT settings, 1%-CBF required over additional 20 h to complete the relaxation process compared with 5%-CBF, indicating a lower polarization potential and more stable diffusion kinetics. Simulated local current density distributions (Fig. 4(e)) further highlight this distinction. The 5%-CBF electrode showed a highly nonuniform current density profile, with large regional differences, whereas the 1%-CBF electrode displayed a more uniform current density across its entire cross-section. These results were directly reflected in the electrochemical performance; 5%-CBF exhibited rapid capacity decay even at a low current density of 0.1 $A \cdot g^{-1}$. Based on its charge–discharge curves (Fig. S21 in the ESM), 5%-CBF maintained a discharge plateau just for the first five cycles. The robust association between structure and performance indicates that the dense sheath layer and poor porosity of 5%-CBF impede sufficient electrolyte wetting and penetration, resulting in elevated ionic diffusion resistance and polarization. Conversely, the 1%-CBF, characterized by its porosity pith layer, promotes consistent ion transport and stable electrochemical kinetics, resulting in enhanced performance.

### 2.4 Synergistic effect of dual-conductive network on electrochemical performance

For battery systems, both ionic conduction pathways and electronic conduction pathways are indispensable. As illustrated in Fig. S22(a) in the ESM, only when both electrons and ions reach the same active site can the electrochemical reaction proceed (e.g., $MnO_2 + 0.5Zn^{2+} + e^- = Zn_{0.5}MnO_2$). Any disruption in either pathway results in increased polarization and degraded battery performance.

In this work, the electronic conductive phase generally consists of carbon-based materials surrounding the electrode or the electrode material itself, while the ionic conductive phase is provided by the electrolyte penetrating into the interior of the electrode. Accordingly, effective electrode design should simultaneously satisfy requirements of electrical conductivity, porosity, and electrolyte affinity. A key distinction between planar batteries and fiber-shaped batteries lies in the available conduction pathways. When non-conductive regions exist within the electrode, planar batteries benefit from multiple conduction directions, whereas fiber batteries rely predominantly on a single conduction direction along the fiber axis (Fig. S22(b) in the ESM). Therefore, constructing a stable and continuous conductive network is more critical for enhancing the performance of fiber-shaped batteries.

As shown in Fig. S22(c) in the ESM, the SCD, optimized only for ionic conduction) electrode exhibits a single conductive pathway. Although the porous pith region allows electrolyte infiltration and thus establishes ionic conduction, the presence of poorly conductive $MnO_2$ disrupts electronic transport, leading to discontinuous electron pathways. In contrast, the DCD electrode, optimized for both ionic and electronic conduction, not only provides unobstructed ionic conduction pathways but also incorporates conductive $MnO_2$ through a composite design, thereby establishing a dual-conductive network. (Fig. S22(d) in the ESM).

To elucidate the importance of constructing electronic and ionic conduction networks simultaneously, we compared the electrochemical performance of fiber electrodes with SCD and DCD. Under identical 1% coagulation bath conditions, the SCD electrode was fabricated using δ-$MnO_2$, while the DCD electrode employed the most conductive composite material, M@C-2.5. As shown in Fig. 5(a), both electrodes displayed low internal resistances ($R_0$) of 6.79 Ω for SCD and 5.52 Ω for DCD. However, their charge-transfer resistances ($R_{ct}$) differ significantly—881.1 Ω for SCD and 384.4 Ω for DCD (Fig. S23 in the ESM). The significantly reduced impedance of DCD arose from the use of highly conductive M@C-2.5, which promoted swift ion and electron transport. Consequently, as shown in Fig. 5(b), the DCD electrode delivers a discharge specific capacity of 343.5 $mAh \cdot g^{-1}$ at 0.1 $A \cdot g^{-1}$, compared with only 113.3 $mAh \cdot g^{-1}$ for the SCD electrode. Under a higher current density of 0.5 $A \cdot g^{-1}$, DCD retained 90.5% of its initial capacity after 100 cycles, whereas SCD suffered severe degradation, decreasing from 77.5 to 37.4 $mAh \cdot g^{-1}$ (Fig. 5(c)). The discharge curves (Fig. 5(d)) demonstrate that DCD preserves stable and distinct voltage plateaus after 100 cycles, but SCD progressively diminishes its plateaus during cycling (Fig. S24 in the ESM). These results highlight the superior electrochemical reversibility and kinetic stability of the dual-conductive system.

To further investigate the underlying electrochemical kinetics, cyclic voltammetry (CV) measurements were performed at scan rates ranging from 1 to 5 $mV \cdot s^{-1}$ (Fig. 5(e)). Both electrodes exhibit characteristic redox peaks corresponding to $Zn^{2+}$ insertion/extraction, but the DCD electrode clearly showed two distinct insertion peaks at low and high potentials (associated with its two voltage plateaus, Fig. S25 in the ESM). Notably, DCD exhibited higher peak currents, smaller polarization voltages, and narrower peak separations than SCD, confirming its faster redox kinetics [41]. The relationship between peak current ($i$) and scan rate ($v$) follows the equation $i = av^b$, where $a$ and $b$ are parameters reflecting the reaction mechanism. When $b = 0.5$, the process is diffusion-controlled, whereas $b = 1.0$ indicates capacitive-dominated behavior. As shown in Fig. S26 in the ESM, fitting results revealed a significantly higher $b$-value for DCD (up to 0.889 for the anodic peak), suggesting that its electrochemical kinetics were less limited by ion diffusion.

Moreover, capacitive contribution analysis (Fig. S27 in the ESM) shows that at 5 $mV \cdot s^{-1}$, the capacitive-controlled ratio reaches 75% for DCD, compared to 68% for SCD, further demonstrating faster charge-transfer dynamics in the DCD system. This conclusion was also supported by GITT measurements (Fig. S28 in the ESM). The average $Zn^{2+}$ diffusion coefficients for SCD and DCD were $6.75 \times 10^{-12}$ and $2.07 \times 10^{-11}$ $cm^2 \cdot s^{-1}$, respectively, indicating that DCD provides abundant electrochemical active sites and shorter ion diffusion paths. In addition, the total duration for relaxation and pulse processes in the DCD was over six times longer than that of SCD, implying lower polarization and more stable ion transport behavior. In terms of rate performance (Fig. 5(f)), the contrast was

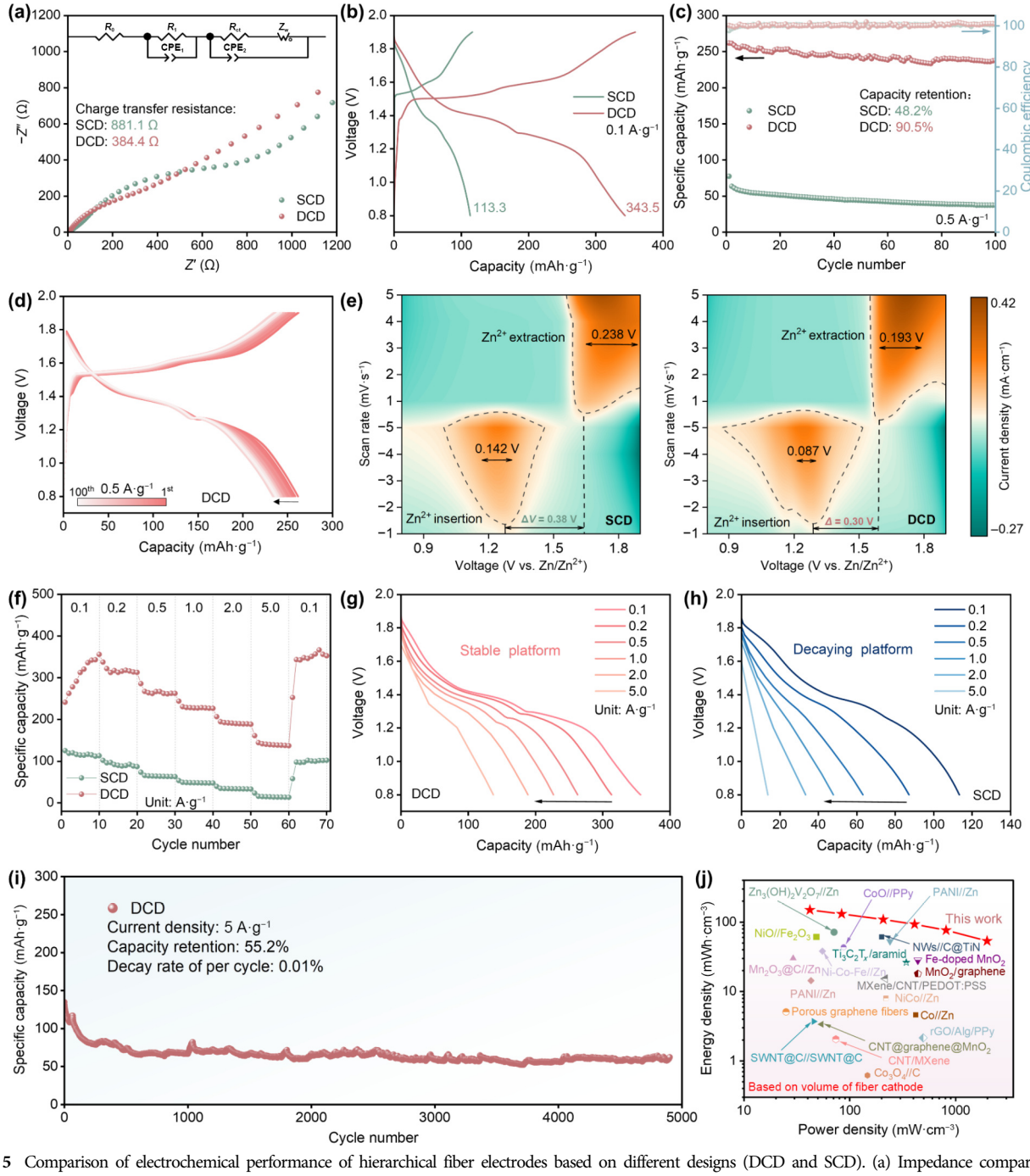


**Figure 5** Comparison of electrochemical performance of hierarchical fiber electrodes based on different designs (DCD and SCD). (a) Impedance comparison. (b) Charge–discharge curves at 0.1 A·g$^{-1}$. (c) Cycling performance comparison at 0.5 A·g$^{-1}$. (d) Charge–discharge curves of DCD for 100 cycles at 0.5 A·g$^{-1}$. (e) Contour plot of CV. (f) Rate performance comparison. (g) Discharge curves of DCD at different current densities. (h) Discharge curves of SCD at different current densities. (i) Long-term cycling performance of DCD at 5 A·g$^{-1}$. (j) Ragone plot of power density and energy density (based on volume of fiber cathode).

even more pronounced. The SCD electrode exhibited extremely poor rate capability, with its capacity approaching 0 mAh·g$^{-1}$ at 5 A·g$^{-1}$, while the DCD electrode maintained high discharge capacities of 230.9, 194.9, and 144.7 mAh·g$^{-1}$ at 1, 2, and 5 A·g$^{-1}$, respectively. This remarkable improvement arises from the enhanced conductivity of the M@C-2.5-based composite, which enables the formation of a continuous electron-conductive network. The corresponding discharge curves (Figs. 5(g) and 5(h)) further confirmed that DCD retains clear voltage plateaus even at 5 A·g$^{-1}$, whereas SCD lost its plateaus beyond 1 A·g$^{-1}$.

To evaluate the long-term durability, cycling stability tests were conducted at a high current density of 5 A·g$^{-1}$. The DCD electrode demonstrated exceptional stability, maintaining 55.2% of its initial capacity after 5000 cycles, with an average decay rate of only 0.01% per cycle (Fig. 5(i)). The Coulombic efficiency (CE) is shown in Fig. S29 in the ESM. Under high current densities, the dissolved Mn tends to redeposit during the charging process, leading to relatively large fluctuations in the CE. According to the dissolution–deposition mechanism, the construction of a porous and electrically conductive substrate is generally required. This also indicates that

the DCD possesses these characteristics, which are beneficial for electrochemical performance. This dissolution–redeposition mechanism may also be one of the reasons for the preserved capacity. Energy and power densities are key parameters for assessing the applicability of fiber-based batteries. As shown in Fig. 5(j), the Ragone plot compares our continuously fabricated FZBs with previously reported advanced fiber energy-storage devices [42–59]. The energy and power densities were calculated based on the volume of the fiber cathode, excluding packaging. Our FZBs achieved a high volumetric energy density of 149.7 mWh·cm$^{-3}$ and a volumetric power density of 42.0 mW·cm$^{-3}$. Even at an ultrahigh power density of 1981.6 mW·cm$^{-3}$, the energy density remained 53.5 mWh·cm$^{-3}$, outperforming many fiber-shaped energy-storage devices reported to date.

### 2.5 Practical demonstration of fiber-shaped zinc batteries

Following the manufacturing design and material optimization, the as-fabricated FZBs exhibit excellent electrochemical performance. However, further evaluation of their mechanical robustness, flexibility, and practical usability is essential to demonstrate their applicability. As shown in Fig. 6(a), the tensile properties of the fiber electrodes were tested (testing setup illustrated in Fig. S30 in the ESM), comparing the performance with and without a metallic core filament. The fiber electrode incorporating the core current

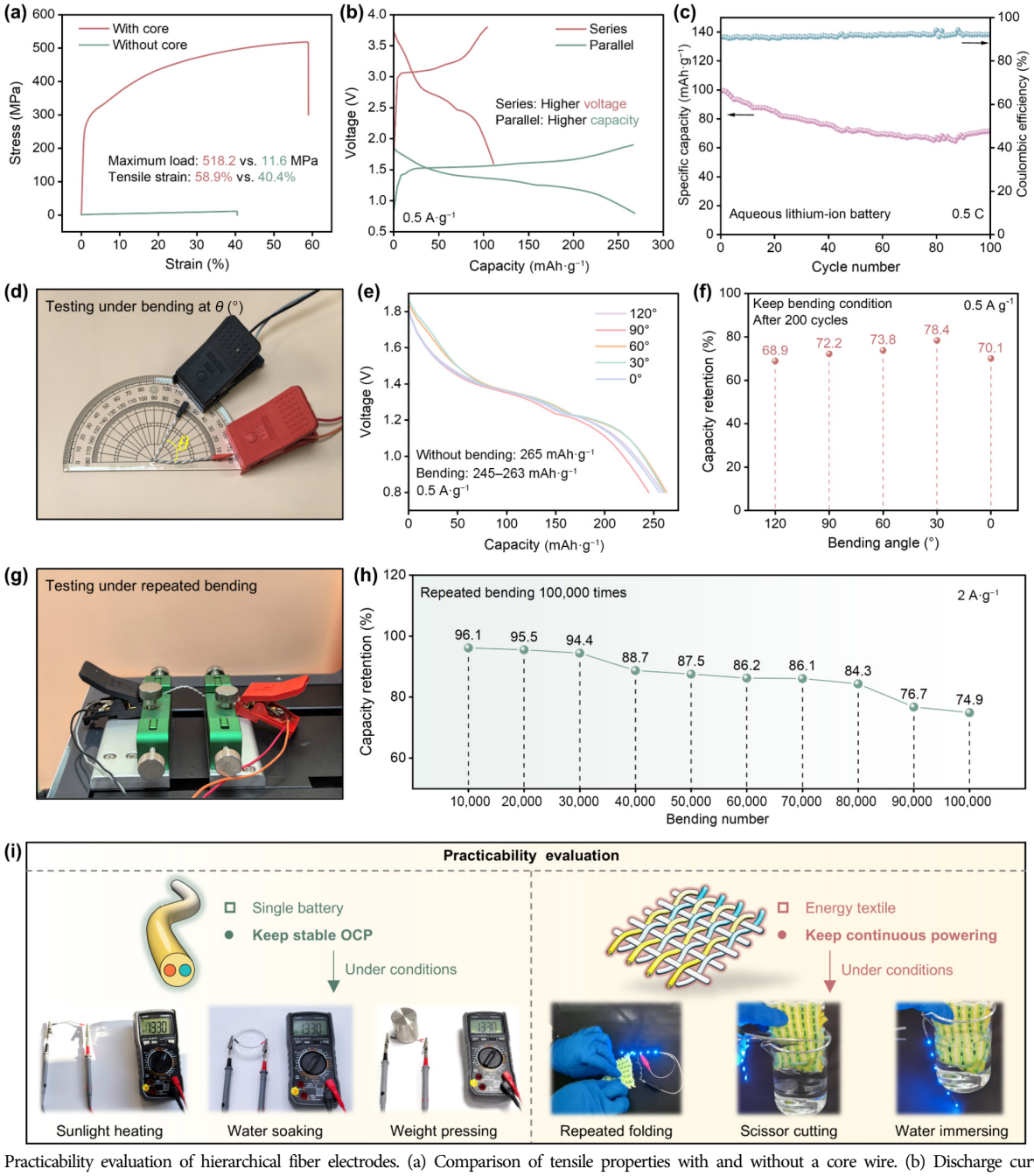


**Figure 6** Practicability evaluation of hierarchical fiber electrodes. (a) Comparison of tensile properties with and without a core wire. (b) Discharge curves under series/parallel connection. (c) Cycling performance of fiber-shaped aqueous lithium-ion battery. (d) Standard for the bending angle. (e) Discharge specific capacity at different bending angles. (f) Capacity retention at different bending angles. (g) Equipment picture of repeated bending test. (h) Capacity retention rate under repeated bending. (i) Practical evaluation of fiber-shaped zinc batteries and energy fabrics.

collector exhibited superior tensile strength (518.2 MPa) and elongation at break (58.9%). In contrast, even the electrode with the highest crosslinking degree but without a core wire showed much lower tensile strength of only 11.6 MPa. These results confirmed that embedding a core filament effectively meets the mechanical strength requirements for fiber-shaped batteries. The core current collector also plays a critical role in providing an efficient pathway for electron transport. Electrodes fabricated without a core collector fail to sustain stable charge–discharge behavior, and even external winding of a collector results in severe polarization (Fig. S31 in the ESM).

To power devices requiring higher voltages or capacities, batteries can be connected in series or parallel configurations. As shown in Fig. 6(b), two FZBs connected in series deliver a voltage of 3.8 V, while a parallel connection doubled the capacity without sacrificing specific capacity compared to a single fiber battery. Both configurations maintain excellent cycling stability, with capacity retentions of 88.3% (series) and 84.3% (parallel) after 200 cycles at 0.5 $A \cdot g^{-1}$ (Fig. S32 in the ESM). To verify the universality of the structural design strategy, it was further extended to fiber-shaped aqueous Li-ion batteries (Fig. 6(c)). The resultant Li-ion fiber batteries had superior electrochemical performance compared to those produced using basic coating techniques (Fig. S33 in the ESM), indicating that the hierarchical core–pith–sheath architecture is universally applicable to diverse fiber energy systems.

Furthermore, the flexibility of the FZBs was systematically evaluated under different bending angles, from nearly folded (0°) to slightly curved (120°) configurations (bending standard shown in Fig. 6(d)). As shown in Fig. 6(e), the discharge capacities ranged from 243 to 263 $mAh \cdot g^{-1}$, close to the unbent state (265 $mAh \cdot g^{-1}$). When cycled under constant bending, the capacity retention remained between 68.9% and 70.1% after 200 cycles (Fig. 6(f)). The electrochemical impedance spectra at different bending angles (Fig. S34 in the ESM) indicated a nearly constant charge-transfer resistance, hence affirming the exceptional flexibility and structural integrity of the fiber electrodes. In actual wearable applications, fiber batteries are necessarily exposed to continuous bending. A 100,000-cycle bending test was therefore performed using a customized repeated bending machine (Fig. 6(g)). As shown in Fig. 6(h), the FZBs maintained a capacity retention of 74.9% after 100,000 bending cycles at 2 $A \cdot g^{-1}$, demonstrating outstanding mechanical durability. This remarkable flexibility may be attributed to the dense outer sheath layer and porous pith layer, which synergistically preserved the external morphology while absorbing internal strain during deformation.

Finally, the environmental stability of the FZBs was evaluated under various conditions (Fig. 6(i)). A single fiber battery maintained a stable open-circuit voltage under prolonged sunlight exposure, water immersion, and mechanical compression. When multiple fiber batteries were woven into energy-storage fabrics, the integrated textile can power light-emitting diode (LED) light strips continuously, even under repeated folding, scissor cutting, and post-cut water immersion (as shown in Video S2 in the ESM). These demonstrations collectively confirmed the exceptional environmental adaptability, mechanical robustness, and practical viability of the fabricated fiber Zn-ion batteries.

## 3 Conclusions

In this work, we designed a scalable wet-spinning method that combines concurrent core wire drawing and slurry solidification to attain the uniform and continuous production of fiber cathodes. By modulating the concentration gradient of the coagulation bath, hierarchical fiber electrodes with an abundant porous structure were achieved, hence constructing the ionic diffusion pathways. Additionally, the electronic conductivity and reactive kinetics of the cathode materials were enhanced by synthesizing $MnO_2$-based composites that simultaneously demonstrated a high specific surface area and substantial pore size. Through comprehensive studies integrating physicochemical characterization, electrochemical testing, and theoretical simulations, we clarified the essential function of constructing interconnected ionic and electronic conduction networks in improving battery performance. The resultant FZBs exhibited a substantial discharge capacity, exceptional rate capability, and remarkable cycling stability. Furthermore, the fiber-shaped Zn-$MnO_2$ batteries had exceptional flexibility and endurance, maintaining continuous functioning under various bending angles and after 100,000 bending cycles, as well as in harsh environments like cutting and water immersion. The scalable wet-spinning technology provides a solid technical foundation for the fabrication of fiber-shaped devices. The universal electrode design strategy offers theoretical support for optimizing high performance fiber-shaped batteries and aims to advance the development of functional fiber electronics and smart textiles.

**Electronic Supplementary Material**: Supplementary material (experimental details, SEM images, XRD patterns, XPS spectra, TEM images, Raman spectra, Brunauer–Emmett–Teller (BET), Micro-CT of fiber or materials, and images and videos of demonstrations) is available in the online version of this article at https://doi.org/10.26599/NR.2026.94908431.

## Data availability

All data needed to support the conclusions in the paper are presented in the manuscript and the Electronic Supplementary Material. Additional data related to this paper may be requested from the corresponding author upon request.

## Acknowledgements

This work was financially supported by the National Natural Science Foundation of China (No. 51702362), the Hunan Provincial Natural Science Foundation (Nos. 2022JJ30663 and 2022JJ40551), the Independent Science Foundation of National University of Defense Technology, and the high-level innovation talent training plan of National University of Defense Technology.

## Declaration of competing interest

All the contributing authors report no conflict of interests in this work.

## Author contribution statement

C. Y. L.: Methodology, investigation, formal analysis, visualization, writing – review & editing. Z. W. J. and Z. Q. Y.: Formal analysis, investigation. Y. J. L., W. W. S., and Q. P. G.: Funding acquisition, project administration. C. M. Z. and S. K. L.: Writing – review & editing, conceptualization, methodology, supervision. All the authors have approved the final manuscript.

## Use of AI statement

None.

## References


[1] Zhou, Z. Y.; Xie, S. J.; Cai, H.; Colli, A. N.; Monnens, W.; Zhang, Q. C.; Guo, W.; Zhang, W.; Han, N.; Pan, H. W. et al. A synchronous-twisting method to realize radial scalability in fibrous energy storage devices. *Sci. Adv.* **2024**, *10*, eado7826.

[2] Ye, L.; Hong, Y.; Liao, M.; Wang, B. J.; Wei, D. C.; Peng, H. S.; Ye, L.; Hong, Y.; Liao, M.; Wang, B. et al. Recent advances in flexible fiber-shaped metal–air batteries. *Energy Storage Mater.* **2020**, *28*, 364–374.

[3] Li, J. B.; Ren, Y. B.; Li, Z.; Huang, Y. H. Phase engineering of nonstoichiometric $Cu_{2-x}Se$ as anode for aqueous Zn-ion batteries. *ACS Nano* **2023**, *17*, 18507–18516.

[4] Li, Q. L.; Zhang, Q. C.; Liu, C. L.; Zhou, Z. Y.; Li, C. W.; He, B.; Man, P.; Wang, X. N.; Yao, Y. G. Anchoring $V_2O_5$ nanosheets on hierarchical titanium nitride nanowire arrays to form core–shell heterostructures as a superior cathode for high performance wearable aqueous rechargeable zinc-ion batteries. *J. Mater. Chem. A* **2019**, *7*, 12997–13006.

[5] Zhang, Q. C.; Li, C. W.; Li, Q. L.; Pan, Z. H.; Sun, J.; Zhou, Z. Y.; He, B.; Man, P.; Xie, L. Y.; Kang, L. X. et al. Flexible and high-voltage coaxial-fiber aqueous rechargeable zinc-ion battery. *Nano Lett.* **2019**, *19*, 4035–4042.

[6] Li, C. W.; Wang, W. H.; Sun, X. J.; Hou, H. L.; Zheng, C.; Zhang, J. C.; Hou, F. J.; Zhang, D. J.; Du, J. M.; Yao, Y. G. Ultra-durable and flexible fibrous mild quasi-solid-state Ag–Zn batteries with $Na_2SO_4$ electrolyte additive. *J. Mater. Chem. A* **2022**, *10*, 24708–24716.

[7] Guan, Q.; Li, Y. P.; Bi, X. X.; Yang, J.; Zhou, J. W.; Li, X. L.; Cheng, J. L.; Wang, Z. P.; Wang, B.; Lu, J. Dendrite-free flexible fiber-shaped Zn battery with long cycle life in water and air. *Adv. Energy Mater.* **2019**, *9*, 1901434.

[8] Cheng, X. Y.; Yang, X.; Zhang, Y. N.; Lv, P. F.; Yang, J. X.; Huang, F. L.; Wei, Q. F. Sulfur vacancies tune the charge distribution of $NiCo_2S_4$ for boosting the energy density of stretchable yarn-based Zn ion batteries. *Adv. Fiber Mater.* **2023**, *5*, 650–661.

[9] Zhang, Y. N.; Wu, D. S.; Huang, F. L.; Cai, Y. B.; Li, Y. G.; Ke, H. Z.; Lv, P. F.; Wei, Q. F. "Water-in-salt" nonalkaline gel polymer electrolytes enable flexible zinc–air batteries with ultra-long operating time. *Adv. Funct. Mater.* **2022**, *32*, 2203204.

[10] Luo, C. Y.; Shao, Y. Y.; Jiang, Z. W.; Pang, M.; Yao, Z. Q.; Li, Y. J.; Sun, W. W.; Shao, Y. L.; Zheng, C. M.; Liu, S. K. Progress in fiber-shaped zinc batteries: From structure, manufacturing, optimization to application. *InfoMat* **2025**, *7*, e70072.

[11] Zhao, C. P.; Wang, R.; Liang, H.; Fang, B.; Li, R. Q.; Wu, R. L.; Mo, R. W. Autonomous self-healing strategy for flexible fiber lithium-ion battery with ultra-high mechanical properties and volumetric energy densities. *Chem. Eng. J.* **2024**, *496*, 154153.

[12] Wu, R. L.; Wei, Y. N.; Wang, R.; Liu, S. X.; Mo, R. W. Nano-interfacial design of self-healable high-strength electrodes with high desalination efficiency and cycling stability. *Chem. Eng. J.* **2025**, *525*, 170242.

[13] Wu, R. L.; Wang, R.; Liu, S. X.; Wang, M. G.; Mo, R. W. Interface-engineered self-healing quasi-solid fiber battery with high energy density and robust mechanical properties. *Adv. Fiber Mater.* **2025**, *7*, 1998–2012.

[14] Wang, R.; Wu, R. L.; Fang, B.; Liang, H.; Mo, R. W. Interface-engineered strategy on carbon nanotubes to chemical stabilize graphene as a self-healing fiber electrode for superior capacitive deionization. *Energy Environ. Mater.*, in press, DOI: 10.1002/eem2.70141.

[15] Su, T. T.; Wang, K.; Chi, B. Y.; Ren, W. F.; Sun, R. C. Stripy zinc array with preferential crystal plane for the ultra-long lifespan of zinc metal anodes for zinc ion batteries. *EcoMat* **2022**, *4*, e12219.

[16] Ahn, Y.; Baek, J.; Kim, S.; Choi, I.; Yoo, J.; Byun, S.; Lee, D. Unveiled mechanism of prolonged stability of Zn anode coated with two-dimensional nanomaterial protective layers toward high performance aqueous Zn ion batteries. *EcoMat* **2024**, *6*, e12482.

[17] Wu, M. H.; Shi, C.; Yang, J. W.; Zong, Y.; Chen, Y.; Ren, Z. G.; Zhao, Y. X.; Li, Z.; Zhang, W.; Wang, L. Y. et al. The $LiV_3O_8$ superlattice cathode with optimized zinc ion insertion chemistry for high mass-loading aqueous zinc-ion batteries. *Adv. Mater.* **2024**, *36*, 2310434.

[18] Guo, J. B.; He, B.; Gong, W. B.; Xu, S. H.; Xue, P.; Li, C. S.; Sun, Y.; Wang, C. L.; Wei, L.; Zhang, Q. C. et al. Emerging amorphous to crystalline conversion chemistry in Ca-doped $VO_2$ cathodes for high-capacity and long-term wearable aqueous zinc-ion batteries. *Adv. Mater.* **2024**, *36*, 202303906.

[19] Wang, N.; Zhai, S. L.; Ma, Y. Y.; Tan, X. H.; Jiang, K. R.; Zhong, W. B.; Zhang, W. Y.; Chen, N.; Chen, W. F.; Li, S. D. et al. Tridentate citrate chelation towards stable fiber zinc-polypyrrole battery with hybrid mechanism. *Energy Storage Mater.* **2021**, *43*, 585–594.

[20] Lu, Y. F.; Zhang, H. J.; Liu, H. D.; Nie, Z. T.; Xu, F.; Zhao, Y.; Zhu, J. X.; Huang, W. Electrolyte dynamics engineering for flexible fiber-shaped aqueous zinc-ion battery with ultralong stability. *Nano Lett.* **2021**, *21*, 9651–9660.

[21] Li, L.; Chen, Y. J.; Wang, S. X.; Pei, D. F.; Li, M. J.; Li, T. X.; Li, C. X. Coaxially spinning stretchable zinc-ion battery fiber with waterproof and scissorability. *Nano Energy* **2024**, *126*, 109662.

[22] Xia, Z.; Li, S.; Wu, G. Q.; Shao, Y. Y.; Yang, D. Z.; Luo, J. R.; Jiao, Z. Y.; Sun, J. Y.; Shao, Y. L. Manipulating hierarchical orientation of wet-spun hybrid fibers via rheological engineering for Zn-ion fiber batteries. *Adv. Mater.* **2022**, *34*, 2203905.

[23] Pu, J.; Cao, Q. H.; Gao, Y.; Wang, Q. Z.; Geng, Z. Y.; Cao, L. Q.; Bu, F.; Yang, N. T.; Guan, C. Liquid metal-based stable and stretchable Zn-ion battery for electronic textiles. *Adv. Mater.* **2024**, *36*, 2305812.

[24] Zhai, S. L.; Wang, N.; Tan, X. H.; Jiang, K. R.; Quan, Z. Y.; Li, Y. W.; Li, Z. Interface-engineered dendrite-free anode and ultraconductive cathode for durable and high-rate fiber Zn dual-ion microbattery. *Adv. Funct. Mater.* **2021**, *31*, 2008894.

[25] Zheng, X. H.; Tang, J. H.; Ding, B. B.; Cao, W. T.; Liu, Z.; Han, X.; Jia, H. Boosting interfacial reaction kinetics in yarn-shaped zinc-$V_2O_5{\cdot}nH_2O$ batteries through carbon nanotube intermediate layer integration. *J. Power Sources* **2024**, *608*, 234618.

[26] Chen, L.; Hu, K. R.; Yang, K.; Yanilmaz, M.; Han, X.; Liu, Y.; Zhang, X. W. A braided flexible Zn–$MnO_2$ yarn battery based on cobweb-like carbonized polypyrrole modified carbon fiber electrodes. *Carbon* **2023**, *215*, 118461.

[27] Li, Y. Y.; Zhang, Y. H.; Yi, J.; Peng, X.; Cheng, R. W.; Ning, C.; Sheng, F. F.; Wang, S.; Dong, K.; Wang, Z. L. Large-scale fabrication of core–shell triboelectric braided fibers and power textiles for energy harvesting and plantar pressure monitoring. *EcoMat* **2022**, *4*, e12191.

[28] Wu, J. J.; Wang, M. X.; Dong, L.; Shi, J.; Ohyama, M.; Kohsaka, Y.; Zhu, C. H.; Morikawa, H. A trimode thermoregulatory flexible fibrous membrane designed with hierarchical core–sheath fiber structure for wearable personal thermal management. *ACS Nano* **2022**, *16*, 12801–12812.

[29] Yu, Y.; Xue, T. T.; Zhu, C. Y.; Zhang, L. S.; Lai, F. L.; Fan, W.; Liu, T. X. High-strength and thermal insulating polyimide aerogel fibers with porous-cortex–dense-core structure enabled by hierarchical phase separation. *Adv. Fiber Mater.* **2025**, *7*, 1605–1614.

[30] Zheng, L. J.; Zhu, M. M.; Wu, B. H.; Li, Z. L.; Sun, S. T.; Wu, P. Y. Conductance-stable liquid metal sheath–core microfibers for stretchy smart fabrics and self-powered sensing. *Sci. Adv.* **2021**, *7*, eabg4041.

[31] Zhang, X. J.; Wang, K.; Hu, J. Y.; Zhang, Y. C.; Dai, Y.; Xia, F. Role of a high calcium ion content in extending the properties of alginate dual-crosslinked hydrogels. *J. Mater. Chem. A* **2020**, *8*, 25390–25401.

[32] Zhou, S.; Guo, K. C.; Bukhvalov, D.; Zhang, X. F.; Zhu, W. Z.; Yao, J. F.; He, M. Cellulose hydrogels by reversible ion-exchange as flexible pressure sensors. *Adv. Mater. Technol.* **2020**, *5*, 2000358.

[33] Bai, J. H.; Wang, R.; Wang, X. M.; Liu, S. D.; Wang, X. L.; Ma, J. M.; Qin, Z. H.; Jiao, T. F. Biomineral calcium-ion-mediated conductive hydrogels with high stretchability and self-adhesiveness for sensitive iontronic sensors. *Cell Rep. Phys. Sci.* **2021**, *2*, 100623.
[34] Wang, Q.; Yang, Y. Q.; Chen, W. C.; Zhang, C.; Rong, K.; Gao, X. Z.; Fan, W. Reliable coaxial wet spinning strategy to fabricate flexible $MnO_2$-based fiber supercapacitors. *J. Alloys Compd.* **2023**, *935*, 168110.
[35] Li, Q. H.; Yuan, Z. H.; Zhang, C.; Hu, S. Q.; Chen, Z. M.; Wu, Y. Z.; Chen, P.; Qi, H. S.; Ye, D. D. Tough, highly oriented, super thermal insulating regenerated all-cellulose sponge-aerogel fibers integrating a graded aligned nanostructure. *Nano Lett.* **2022**, *22*, 3516–3524.
[36] Gao, T. T.; Yan, G. Y.; Yang, X.; Yan, Q.; Tian, Y. K.; Song, J. W.; Li, F. X.; Wang, X. L.; Yu, J. Y.; Li, Y. J. et al. Wet spinning of fiber-shaped flexible Zn-ion batteries toward wearable energy storage. *J. Energy Chem.* **2022**, *71*, 192–200.
[37] Wang, Y. B.; Chen, C. J.; Xie, H.; Gao, T. T.; Yao, Y. G.; Pastel, G.; Han, X. G.; Li, Y. J.; Zhao, J. P.; Fu, K. et al. 3D-printed all-fiber Li-ion battery toward wearable energy storage. *Adv. Funct. Mater.* **2017**, *27*, 1703140.
[38] Du, Z. C.; Zha, Q. B.; Zhang, Z. H.; Chen, Q.; Yang, H.; Lu, Z. G.; Zhai, T. Y.; Li, H. Q. An efficient thick electrode design with artificial porous structure and gradient particle arrangement for lithium-ion batteries. *Energy Environ. Mater.* **2025**, *8*, e12867.
[39] Zheng, X. H.; Cai, J. M.; Cao, Y. N.; Shen, L. J.; Zheng, Y.; Liu, F. J.; Liang, S. J.; Xiao, Y. H.; Jiang, L. L. Construction of cross-linked δ-$MnO_2$ with ultrathin structure for the oxidation of $H_2S$: Structure–activity relationship and kinetics study. *Appl. Catal. B: Environ.* **2021**, *297*, 120402.
[40] Xu, Z. H.; Pang, Z. B.; Alshammari, S.; Yan, X. F.; Thabet, H. K.; Jiang, X. H.; El-Bahy, Z. M.; Xu, X. T.; Yu, L. M. Ultrathin $MnO_2$ nanosheets/carbon nanotubes heterostructures via electrostatic self-assembly for high-efficiency capacitive deionization. *Chem. Eng. J.* **2025**, *522*, 166426.
[41] Li, H.; Chuai, M. Y.; Xiao, X.; Jia, Y. Y.; Chen, B.; Li, C.; Piao, Z. H.; Lao, Z. J.; Zhang, M. T.; Gao, R. H. et al. Regulating the spin state configuration in bimetallic phosphorus trisulfides for promoting sulfur redox kinetics. *J. Am. Chem. Soc.* **2023**, *145*, 22516–22526.
[42] Pan, Z. H.; Yang, J.; Zhang, Q. C.; Liu, M. N.; Hu, Y. T.; Kou, Z. K.; Liu, N.; Yang, X.; Ding, X. Y.; Chen, H. et al. All-solid-state fiber supercapacitors with ultrahigh volumetric energy density and outstanding flexibility. *Adv. Energy Mater.* **2019**, *9*, 1802753.
[43] Zhou, C.; Zhang, Y. W.; Li, Y. Y.; Liu, J. P. Construction of high-capacitance 3D CoO@polypyrrole nanowire array electrode for aqueous asymmetric supercapacitor. *Nano Lett.* **2013**, *13*, 2078–2085.
[44] Zhang, Y.; Wang, Y. H.; Wang, L.; Lo, C. M.; Zhao, Y.; Jiao, Y. D.; Zheng, G. F.; Peng, H. S. A fiber-shaped aqueous lithium ion battery with high power density. *J. Mater. Chem. A* **2016**, *4*, 9002–9008.
[45] Wang, X. F.; Liu, B.; Liu, R.; Wang, Q. F.; Hou, X. J.; Chen, D.; Wang, R. M.; Shen, G. Z. Fiber-based flexible all-solid-state asymmetric supercapacitors for integrated photodetecting system. *Angew. Chem.* **2014**, *126*, 1880–1884.
[46] Liu, J. P.; Guan, C.; Zhou, C.; Fan, Z.; Ke, Q. Q.; Zhang, G. Z.; Liu, C.; Wang, J. A flexible quasi-solid-state nickel–zinc battery with high energy and power densities based on 3D electrode design. *Adv. Mater.* **2016**, *28*, 8732–8739.
[47] Meng, Q. H.; Wu, H. P.; Meng, Y. N.; Xie, K.; Wei, Z. X.; Guo, Z. X. High performance all-carbon yarn micro-supercapacitor for an integrated energy system. *Adv. Mater.* **2014**, *26*, 4100–4106.
[48] Guan, C.; Zhao, W.; Hu, Y. T.; Ke, Q. Q.; Li, X.; Zhang, H.; Wang, J. High performance flexible solid-state Ni/Fe battery consisting of metal oxides coated carbon cloth/carbon nanofiber electrodes. *Adv. Energy Mater.* **2016**, *6*, 1601034.
[49] Wang, H. M.; Wang, C. Y.; Jian, M. Q.; Wang, Q.; Xia, K. L.; Yin, Z.; Zhang, M. C.; Liang, X. P.; Zhang, Y. Y. Superelastic wire-shaped supercapacitor sustaining 850% tensile strain based on carbon nanotube@graphene fiber. *Nano Res.* **2018**, *11*, 2347–2356.
[50] Jin, Z. Y.; Li, P. P.; Jin, Y.; Xiao, D. Superficial-defect engineered nickel/iron oxide nanocrystals enable high-efficient flexible fiber battery. *Energy Storage Mater.* **2018**, *13*, 160–167.
[51] Huang, Y.; Ip, W. S.; Lau, Y. Y.; Sun, J. F.; Zeng, J.; Yeung, N. S. S.; Ng, W. S.; Li, H. F.; Pei, Z. X.; Xue, Q. et al. Weavable, conductive yarn-based NiCo//Zn textile battery with high energy density and rate capability. *ACS Nano* **2017**, *11*, 8953–8961.
[52] Hang, G. G.; Liu, Z.; Zhang, J.; Wang, Y. N.; Meng, W.; Li, Y.; Wang, X. C. Microstructural design of 3D intertwined biomimetic composite fibers for functional smart textiles in energy storage. *Small* **2025**, *21*, e04594.
[53] Oh, S.; Lee, S.; Kim, H.; Song, Y. C.; Kim, H.; Lee, Y.; Lim, S. C.; Suh, D.; Kim, S. H.; Kim, K. J. Reduced graphene oxide composite fiber with hierarchical pores for all-solid-state fiber supercapacitors. *Carbon* **2025**, *234*, 119998.
[54] Ding, T.; Jiang, X. P.; Quan, J. X.; Wang, R.; Li, W. F.; Li, M.; Lan, C. T.; Ma, W. J.; Zhu, M. F. Scalable fabrication of hierarchically porous graphene fibers via hydrothermal self-assembly and GO-assisted wet-spinning for high performance flexible supercapacitors. *Carbon* **2025**, *239*, 120326.
[55] Jorn-am, T.; Kim, C. H.; Chanthad, C.; Paoprasert, P.; In, I.; Lee, S. Y.; Park, S. J. Scalable interfacial design of CNT/MXene hybrid yarns for durable and flexible supercapacitors. *Small* **2025**, *21*, e08739.
[56] Cheng, X. Y.; Tian, X. J.; Liao, S. Q.; Wang, Q. Q.; Wei, Q. F. Wet spinning for high performance fiber supercapacitor based on Fe-doped $MnO_2$ and graphene. *Carbon* **2024**, *230*, 119572.
[57] Tian, X. J.; Cheng, X. Y.; Liao, S. Q.; Chen, J. F.; Lv, P. F.; Wei, Q. F. High electrochemical capacity $MnO_2$/graphene hybrid fibers based on crystalline regulatable $MnO_2$ for wearable supercapacitors. *ACS Appl. Mater. Interfaces* **2023**, *15*, 52415–52426.
[58] Liu, Q.; Zhao, A. R.; He, X. X.; Li, Q.; Sun, J.; Lei, Z. B.; Liu, Z. H. Full-temperature all-solid-state $Ti_3C_2T_x$/aramid fiber supercapacitor with optimal balance of capacitive performance and flexibility. *Adv. Funct. Mater.* **2021**, *31*, 2010944.
[59] Shi, H.; Chen, S.; Shi, W.; Peng, Z. F.; Li, J. Y.; Liu, Z. L.; Zhang, G. Y.; Liu, L. High performance fiber-shaped supercapacitors based on core–shell fiber electrodes with adjustable surface wrinkles and robust interfaces. *J. Mater. Chem. A* **2021**, *9*, 16852–16859.

This is an open access article under the terms of the Creative Commons Attribution 4.0 International License (CC BY 4.0, https://creativecommons.org/licenses/by/4.0/).

© The Author(s) 2026. Published by Tsinghua University Press.